Design and Analysis of Guided Surface Acoustic Waves in ScAlN on Sapphire for Phononic Integrated Circuits

Jack Guida , *Graduate Student Member, IEEE*, and Siddhartha Ghosh , *Member, IEEE*

***Abstract*—This study presents a comprehensive dispersion analysis and characterization of guided surface acoustic waves (SAWs) in 30% scandium aluminum nitride (ScAlN) alloy thin films on sapphire. The solidly mounted platform, which supports the fundamental Rayleigh and Sezawa SAW modes, offers mechanical robustness and high electromechanical coupling (k^2_t), while maintaining high confinement of the acoustic modes. Numerical modeling, coupled with experimental results, showcases the characteristics of focusing interdigitated transducers (FIDTs) for injecting acoustic energy into piezoelectric etch-defined acoustic waveguides and highlights their advantages over conventional uniform aperture transducers. Identity mapping of boundary conditions significantly reduces degrees of freedom (DoFs) in modeling energy injection into acoustic waveguides. The theory of Gaussian beams in optics is applied to the FIDTs to model the physical response of the transducers accurately and emphasize their high-intensity focusing nature. This work also demonstrates the ability of FIDTs to facilitate phononic devices and phononic integrated circuit (PnICs) applications in slow-on-fast piezoelectric platforms.**

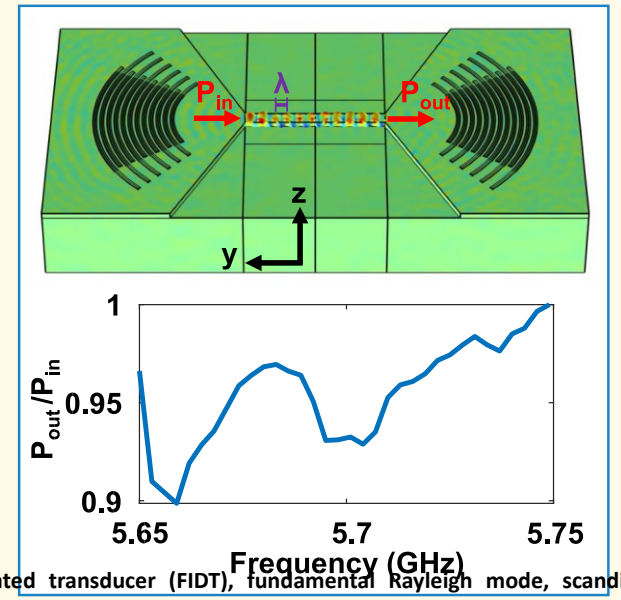

***Index Terms*—Acoustic waveguide, dispersion, focusing interdigitated transducer (FIDT), fundamental Rayleigh mode, scandium aluminum nitride (ScAlN) on sapphire, Sezawa mode.**

I. Introduction

THE development of surface acoustic wave (SAW) devices in piezoelectric platforms for radio frequency (RF) systems has propelled modern wireless communication [1] and is a gateway to the next generation of telecommunications [2], [3]. When converting electromagnetic signals into the mechanical domain through the piezoelectric effect, the phase velocity decreases by roughly five orders of magnitude for a given operating frequency, implying the wavelength decreases on the same order of magnitude. This allows for the miniaturization of RF front ends for compact signal processing systems using acoustic wave technology, with applications in filters [4], sensors [5], oscillators [6], correlators [7], [8], circulators [9], duplexers [10], and other nonreciprocal networks [11], [12], [13].

Received 11 July 2024; accepted 16 October 2024. Date of publication 21 October 2024; date of current version 27 January 2025. This work was supported in part by the Defense Advanced Research Projects Agency through the Young Faculty Award (YFA) Program under Grant D24AP00005. *(Corresponding author: Jack Guida.)*

The authors are with the Department of Electrical and Computer Engineering, Northeastern University, Boston, MA 02115 USA (e-mail: guida.j@northeastern.edu; s.ghosh@northeastern.edu).

Digital Object Identifier 10.1109/TUFFC.2024.3484181

Surface acoustic waves (SAWs) and SAW-based devices occur in both multilayer substrates [15], [16]. For the latter, SAW-based devices are enabled by acoustic waveguiding, which occurs when the piezoelectric material has a slower phase velocity compared with the substrate it lies on. This change in acoustic impedance confines the mode and minimizes energy leakage into the substrate, enabling low-loss guided acoustic wave devices [17]. In addition, the slow-on-fast configuration allows for the propagation of the first higher order SAW mode, the Sezawa mode [18], which has also been referred to as a guided Lamb wave [19], [20]. The higher order mode, inherently having a higher phase velocity, permits dual frequency operation for the same lithographic constraints.

ScAlN alloy thin films have become a popular piezoelectric material thanks to their enhanced piezoelectric coefficients [21] compared with aluminum nitride (AlN). Lamb waves in ScAlN have higher theoretical electromechanical coupling (k_t^2) than that of solidly mounted SAWs [22], but bulk piezoelectric materials [14] and composite

Authorized licensed use limited to: Northeastern University. Downloaded on January 29,2025 at 17:02:16 UTC from IEEE Xplore. Restrictions apply.

1525-8955 © 2024 IEEE. Personal use is permitted, but republication/redistribution requires IEEE permission. See https://www.ieee.org/publications/rights/index.html for more information.

Highlights

- **This work presents numerical modeling of 30% ScAlN on sapphire that predicts SAW dispersion and focusing characteristics of FIDTs for guided SAWs, while reducing the DoFs through identity mapping.**
- **Experimentally verified dispersion and focusing effects in the SoS platform show the superior performance compared with conventional IDTs.**
- **Focusing transducers, offering higher energy injection into etch-defined waveguides, make them highly suitable for advanced phononic devices and PnICs applications.**

the necessity for these films to exist in suspended plates limits their mechanical robustness and integration ability for large-scale phononic devices. The deposition of ScAlN on sapphire substrates enables a relatively low-cost slow-on-fast SAW platform which has shown to improve the microwave signal processing capabilities [23] compared with AlN.

Waveguiding using a piezoelectric material in multilayer platforms introduces the ability to further confine the acoustic mode through modifying in-plane boundary conditions, leading to the spatial routing and control of acoustic waves in a manner similar to the photonic domain [24]. This full 3-D control has had applications in RF front-end signal processing using phononic integrated circuits (PnICs) [19], [25] and integrated optomechanics for waveguides with the support of both optical and acoustic modes [26]. One method of imposing the necessary boundary conditions for the in-plane spatial control is the use of phononic crystals. The formation of a bandgap enables acoustic confinement, but requires a large physical area and a challenging fabrication process. The effective translation from the photonic-to-phononic domain motivates the search for other methods for wavelength scale conversion of acoustic modes [27].

The interdigitated transducer (IDT) used to excite acoustic modes in piezoelectric films requires large electrode apertures to match to 50-Ω systems. Moreover, the IDT produces a mode profile that provides extreme difficulty in a conversion of power on a wavelength scale, which is necessary for large scale PnICs [28]. Conversely, focusing interdigitated transducers (FIDTs) have led to the miniaturization of PnICs through wavelength scale confinement of acoustic waves in piezoelectric platforms [19] with sufficient impedance matching for RF networks [29]. The focusing nature of the transducer allows for physical routing and full spatial control of these modes through piezoelectric etch-defined acoustic waveguides [30]. The ability to focus acoustic energy into a waveguide allows for the interconnection of intricate phononic devices for fully integrated phononic circuit elements with complex functionalities. This article presents a numerical modeling technique coupled with theoretical and experimental analysis to compare transducer designs on the 30% ScAlN on sapphire (SoS) platform for the improvement of PnIC technology. This article is organized as follows. In Section II, slow-on-fast piezoelectric platforms are conceptually and analytically described as well as applied to the SoS platform for the demonstration of higher order modes. Section III presents the dispersion analysis of the SoS platform through numerical simulations while looking at different means of optimizing electromechanical coupling. In Section IV, the motivation for using FIDTs compared with standard IDTs for the mode conversion into an acoustic waveguide is numerically presented. Section V analyzes the experimental results of acoustic delay lines (ADLs) to characterize propagation characteristics and performance in the SoS platform. Finally, the conclusion of this work is presented in Section VI.

II. Slow-on-Fast Piezoelectric Platforms

Slow-on-fast platforms refer to the layering of a slower phase velocity piezoelectric thin film on top of a faster phase velocity substrate. This also allows for the large-scale integration of mechanically robust phononic circuit components. The phase velocity of the composite platform is determined by the properties of the piezoelectric film with respect to the substrate it is deposited on. One slow-on-fast geometry configuration is shown in Fig. 1(a) with a lateral field excitation (LFE) electrode structure, along with the total displacement plotted along the cross section of the device, demonstrating the mode profile for the fundamental Rayleigh and Sezawa modes. The Sezawa mode is the first higher order mode of the fundamental Rayleigh and is an overtone with two coupled components of transverse and longitudinal waves. The Sezawa mode inherently relies on the piezoelectric coefficients e_{31} and e_{33} and causes the transverse component to penetrate into the substrate. Thus, the Sezawa mode only propagates when slow-on-fast conditions are met [31]. The alloying of AlN with scandium decreases the phase velocity of acoustic modes in ScAlN, and allows for the slow-on-fast condition to be satisfied in the SoS platform, enabling the use of both Rayleigh and Sezawa modes in the material stack.

Slowness curves or inverse velocity curves describe the propagation characteristics of plane waves in elastic materials. Using the Christoffel equation for a given material based on its point group, a dispersion relation is obtained by setting the characteristic determinant equal to 0. At a fixed frequency (ω), the dispersion relation defines a surface in k-space called the wave vector surface, which expresses the acoustic wave vector

Authorized licensed use limited to: Northeastern University. Downloaded on January 29,2025 at 17:02:16 UTC from IEEE Xplore. Restrictions apply.

k as a function of direction. Instead, the relationship can be defined in terms of k/ω, which considers the slowness (also known as the inverse velocity) surface rather than the wave vector surface, which scales with ω [17].

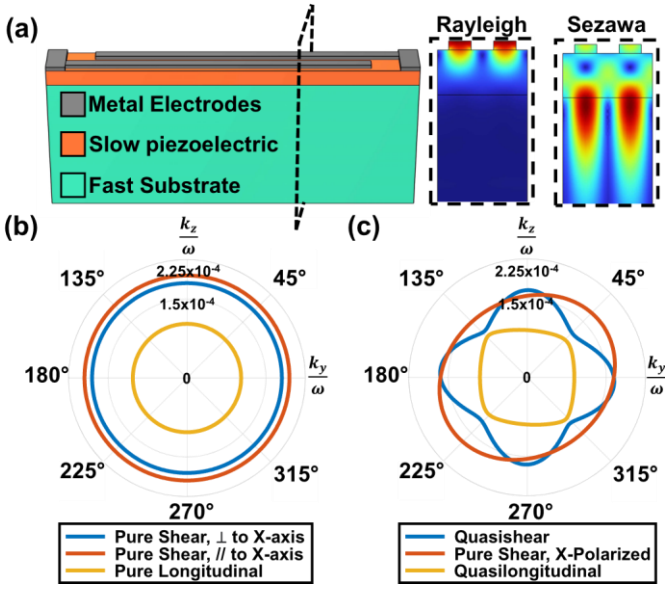

Fig. 1. (a) Slow-on-fast piezoelectric platform configuration. Closed form solution slowness (inverse velocity) curves for (b) ScAlN with propagation in the XY plane and (c) sapphire with propagation in the YZ plane.

Sapphire falls under the 3-m trigonal (or rhombohedral) point group, and the characteristic equation derived from the Christoffel matrix factors only for propagation in the Y Z plane or for propagation along the X-, Y-, and Z-axes, with each axis corresponding to the [100], [010], and [001] planes. ScAlN falls under the hexagonal crystal class and the characteristic equation factors when propagation is in the XY plane. These slowness curves are a function of the material's elastic constants taken from [21] and [32] for 30% ScAlN and sapphire, respectively. The slowness curves for 30% ScAlN and sapphire based on the solution to their respective Christoffel equations are shown in Fig. 1(b) and (c), respectively. Although certain planes have a closed form solution, the fabricated 30% SoS stack consists of ScAlN with c-plane orientation deposited on c-plane sapphire, which corresponds to propagation normal to Z. The phase velocities for both ScAlN and sapphire with propagation normal to Z are summarized in Table I, which includes the slowest phase velocity for sapphire to define a limiting case. The table demonstrates that at every orientation with propagation normal to the c-axis, the slow-onfast condition is satisfactory for the SoS material stack. In 30% ScAlN, $(k/\omega)_1$, $(k/\omega)_2$, and $(k/\omega)_3$ correspond to modes that are purely shear polarized parallel to the Z-axis, purely shear polarized perpendicular to the Z-axis, and purely longitudinal, respectively. For sapphire, these correspond to two quasi-shear modes and a quasi-longitudinal mode. This analysis shows that the same one-mask LFE electrode configuration in the SoS slow-on-fast platform will support two SAW modes at two different operating frequencies for the same lithographic constraints, which has also been shown experimentally [33].

III. Dispersion Analysis

The dispersive behavior of plane waves describes how the propagation characteristics of those waves change over their operating frequency. SAWs are inherently frequency dispersive due to IDT electrode widths being comparable with the SAW wavelength [34]. The propagation characteristics of the launched acoustic wave directly contribute to the device performance. The electromechanical coupling (k_t^2) is a key device metric for acoustic wave devices since it modulates the equivalent motional resistance, and therefore, loss in the device [1]. The electromechanical coupling is defined as $k_t^2 = (\pi^2/4)(1 - (f_s/f_p))$ [35], where f_s and f_p are the series and parallel resonant frequencies (corresponding to the modified Butterworth-Van Dyke equivalent model). The coupling, being a function of resonant and parallel frequencies, depends on the phase velocities of the SAW modes. The phase velocity therefore plays a powerful role in ensuring a slow-on-fast platform and an optimized device performance.

TABLE I
Mode Phase Velocity Extraction From Slowness Curves in 30% ScAlN and Sapphire

	30% ScAlN	Sapphire
$\left(\frac{k}{\omega}\right)_1$	$\sqrt{\frac{\rho}{c_{44}}}$	$\sqrt{\frac{2\rho}{c_{11}+c_{44}-\sqrt{(c_{11}-c_{44})^2+4c_{14}^2}}}$
$\left(\frac{k}{\omega}\right)_2$	$\sqrt{\frac{\rho}{c_{66}}}$	$\sqrt{\frac{2\rho}{c_{44}+c_{66}-\sqrt{(c_{66}-c_{44})^2+4c_{14}^2}}}$
$\left(\frac{k}{\omega}\right)_3$	$\sqrt{\frac{\rho}{c_{11}}}$	$\sqrt{\frac{\rho}{c_{11}}}$
v_1	5,547 m/s	6,038 m/s
v_2	5,136 m/s	5,736 m/s
v_3	9,716 m/s	11,145 m/s

A. Numerical Analysis for Coupling Performance in SoS

COMSOL Multiphysics Finite Element Method (FEM) simulation is used to study the dispersive nature of the SAW modes through frequency domain analysis of the SoS platform. A 2-D unit cell consisting of 400 nm of 30% ScAlN on a sapphire substrate is utilized for extracting the admittance response over different operating frequencies (defined through electrode lithography), given the same piezoelectric film thickness. The material stack has an LFE configuration, similar to what is shown in the cross section of Fig. 1(a). The electrodes consist of aluminum with a thickness that yields a constant $t_m/\lambda = 0.1$, where t_m is the metal electrode thickness and λ is the operating wavelength. As this wavelength (and consequently the operating frequency) is swept, the ratio of the piezoelectric film thickness (t) with respect to the acoustic

Authorized licensed use limited to: Northeastern University. Downloaded on January 29,2025 at 17:02:16 UTC from IEEE Xplore. Restrictions apply.

wavelength (λ) becomes an important device metric, given by t/λ. An electrode coverage of 0.5 is used for all frequencydomain simulations.

The electromechanical coupling is extracted over a t/λ sweep from 0.05 to 1 for both the fundamental Rayleigh and Sezawa modes and is plotted in Fig. 2(a). The phase velocity for these propagating modes is plotted over the operating frequency, as shown in Fig. 2(b). This helps demonstrate the dispersive nature of both modes, showing how the phase velocity for both decreases as the operating frequency

Authorized licensed use limited to: Northeastern University. Downloaded on January 29,2025 at 17:02:16 UTC from IEEE Xplore. Restrictions apply.

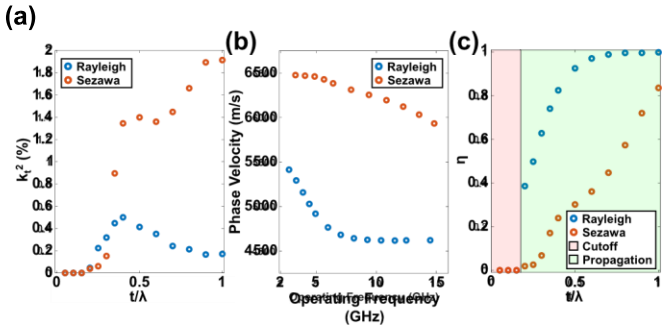

Fig. 2. (a) Effective electromechanical coupling (k^2_t) over the ratio of film thickness with respect to the operating acoustic wavelength (t/λ). (b) Phase velocity over operating frequency demonstrating the mild dispersive behavior of the SAW modes. (c) Mode confinement (η) for both the fundamental Rayleigh and Sezawa modes over t/λ, showcasing the dispersive behavior in the performance of confining the SAW.

increases. The fundamental Rayleigh mode quickly reaches a constant phase velocity over operating frequency compared with the Sezawa mode. The greater difference in acoustic phase velocity between the piezoelectric layer and substrate in slow-on-fast platforms increases the device performance as the mode is confined more within the piezoelectric film and minimizes leakage, as the material stack ideally approaches the boundary conditions of a suspended plate [36]. This implies that as the operating frequency increases and phase velocity decreases, more of both SAW modes will be confined. To quantitatively evaluate the mode confinement, an energy efficiency ratio η is defined such that

$$\eta = \frac{\int_{E+P} W(x, y)\, dA}{\int_{E+P+S} W(x, y)\, dA}. \quad (1)$$

In (1), $W(x, y)$ represent the elastic strain energy density field, and E, P, and S represent the domains of the electrodes, piezoelectric film, and substrate, respectively. Equation (1) shows the ratio that defines the elastic strain energy in the piezoelectric and electrodes with respect to the elastic strain energy in the entire material stack, giving an indication of confinement versus leakage, which has also been observed with leaky SAWs [37]. This energy confinement ratio η is plotted over t/λ in Fig. 2(c), demonstrating a cutoff for higher order SAW modes. Although the coupling may approach 0, the fundamental Rayleigh mode can propagate in the SoS platform over all frequencies, where the Sezawa mode exists only above a cutoff frequency. Sapphire can be approximated as a hexagonal crystal [38], which gives a transverse phase velocity of $v_2 = c_{66}/\rho \approx 6450$ m/s for the mode polarized perpendicular to the axis that is normal to the surface, which is the component that shows up in the Sezawa mode but is absent in the fundamental Rayleigh. Fig. 2(b) and (c) shows that as the operating frequency decreases and the phase velocity of the Sezawa mode increases, the mode becomes cutoff roughly around this value of the pure shear mode that occurs when sapphire is approximated as hexagonal. As the phase velocity of both the fundamental Rayleigh and Sezawa modes decrease, there is a drastic increase in the energy confinement ratio, where η approaches unity as t/λ approaches 1. Reaching higher t/λ ratios for a fixed film thickness requires finer resolution of lithographic features, but is extremely important in terms of device performance based on the dispersive nature of the modes.

B. Electrode Material and Configuration on Coupling Performance

It was previously shown that the piezoelectric film thickness with respect to acoustic wavelength (t/λ) plays a significant role in electromechanical coupling and the operational characteristics of SAWs based on mode dispersion. There have been methods of optimizing device performance in terms of k_t^2 that rely on changing metal type and electrode configuration. Using denser metal has shown to provide a stronger mass loading effect on the phase velocity of SAWs. Mass loading due to these denser metals decreases the phase velocity of the acoustic modes, and therefore is desirable for slow-on-fast platforms, while also increasing k_t^2 by an amount proportional to the difference in acoustic impedance between the metal and piezoelectric film [39], [40].

Gold is a denser metal than aluminum, and in leaky SAW applications, the mass loading effect has shown to transfer a greater amount of strain into the electrodes. Bringing the mode closer to the surface of the piezoelectric material increases mode confinement [37] and slows down the phase velocity, which is important for cutoff with the Sezawa mode. Simultaneously, a key metric for traveling acoustic wave devices in RF systems is insertion loss, which is limited by the electromechanical coupling. For the SoS platform, different electrode configurations with gold as the electrode metal are evaluated for the optimization of coupling and phase velocity for a sweep of t/λ, with an analysis done for the fundamental Rayleigh and Sezawa modes.

Lateral field, thickness field, and floating bottom electrodes [41] configurations are used to optimize coupling for the same material stack of 400 nm of 30% SoS. For the scenarios in which a bottom electrode is present (TFE and FBE), platinum was used with a thickness of 20 nm. Electrode thicknesses are kept again at a constant $t_m/\lambda = 0.1$. The results for showcasing improved k_t^2 over t/λ for the fundamental Rayleigh and Sezawa modes are shown in Fig. 3(a) and (b), respectively. Comparing against aluminum LFE electrodes, it is immediately clear the denser metal significantly improves device performance in terms maximum coupling reached for all electrode configuration types. Gold, being a denser metal and reducing the phase velocity of both SAW modes, increases

Authorized licensed use limited to: Northeastern University. Downloaded on January 29,2025 at 17:02:16 UTC from IEEE Xplore. Restrictions apply.

(a)

the difference in acoustic impedance between the piezoelectric and substrate allowing for higher coupling for both modes and a lower cutoff frequency for the Sezawa mode. Fig. 3 additionally demonstrates that if maximum coupling is desired; the operating wavelength and electrode configuration must be considered.

The absolute peak in the coupling for both SAW modes occurs roughly at a $t/\lambda = 0.2$ for the TFE and FBE configurations. This follows the trend seen with the Lamé mode resonators, in which the bidimensionality of higher order modes allows for the maximization of coupling between the electric field and mechanical stress/strain fields through

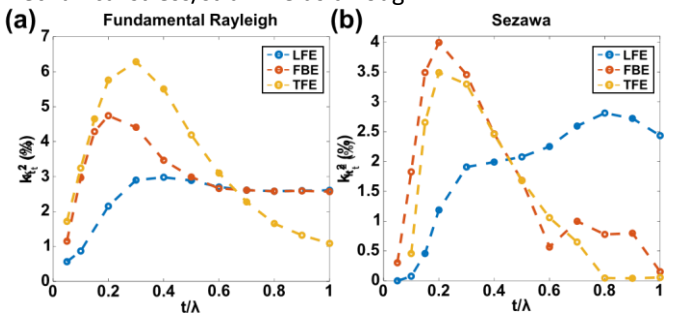

Fig. 3. Effective electromechanical coupling, k^2_t, over t/λ with various gold electrode configurations [lateral field excitation (LFE), floating bottom excitation (FBE), and thickness field excitation (TFE)] for (a) fundamental Rayleigh and (b) Sezawa SAWs.

electrode configuration [42]. Coupling at its optimal point is higher in the case of the fundamental Rayleigh compared with the Sezawa, contrary to the aluminum LFE case. Since both modes reach their optimal coupling at roughly the same t/λ, for this corresponding design wavelength two different frequency bands can be utilized for the same transducer design, which can be impactful if frequency scaling is a necessity [43]. Overall, the electrode configuration and material can be chosen to optimize the dispersion and enhance slow-on-fast conditions in SoS to maximize electromechanical coupling.

IV. Numerical Modeling for Phononic Components

PnICs use an acoustic waveguide to confine a propagating acoustic wave with control in all three dimensions [44]. The 2-D spatial manipulation and routing as well as the vertical confinement of the acoustic wave allow for the implementation of intricate functions that motivates all-acoustic RF signal processing systems. Solidly mounted PnICs offer a mechanical robustness and stability that is not easily feasible in suspended platforms [45]. PnICs in solidly mounted platforms rely on the slow-on-fast concept, with different applications of waveguiding techniques, such as strip, rib, and overlay slot waveguides, which all rely on the piezoelectric material having the slowest phase velocity with reference to the material stack [46].

Numerical modeling techniques coupled with the physical theory can allow for an effective quantitative analysis and optimal device design in PnIC platforms. COMSOL Multiphysics is used to develop a library of devices that, in the acoustic domain, functions analogously to devices in the photonic domain. In a comprehensive library of phononic components, fundamental concepts such as wavelength-scale mode conversion and waveguiding are thoroughly analyzed to inform design considerations.

The SoS platform, as previously seen, satisfies the slow-on-fast conditions but the phase velocities of the piezoelectric material and the substrate are near each other. Even the optimized operating t/λ regime leads to relatively low electromechanical coupling, which can impact the overall performance of SAW devices. Lithium niobate is a very high electromechanical coupling piezoelectric material [47] that has a low phase velocity when integrated on solidly mounted platforms, such as lithium niobate on silicon, quartz [16], sapphire [48], silicon carbide [15], and diamond [49]. Although it has excellent coupling, it requires wafer-bonding techniques and is highly anisotropic, whereas ScAlN is isotropic inplane. Thus, the SoS platform is used as a means to prove the potential of the FIDT for intricate phononic components, starting with a novel numerical modeling technique.

A. Focusing Interdigitated Transducer

A fundamental feature of PnICs lies in the ability to generate a wavelength-scale conversion of an acoustic mode, allowing for the miniaturization of these systems. Standard IDTs with implementation in RF systems need relatively large electrode apertures to comply with 50-Ω impedance matching for insertion loss maximization, with the mode profile produced on the same order as the aperture itself. For practical applications, the use of conventional IDTs for injecting acoustic energy into a wavelength-scale acoustic waveguide has shown limitations due to mismatch in aperture length of the IDT and waveguide. There have also been attempts to deposit electrodes directly onto the waveguide itself, which results in a challenging fabrication process and leads to an extremely narrow bandwidth because of the large number of electrode pairs required for impedance matching [50]. Ultimately, the transducer aperture needs to be on the order of the waveguide dimension to minimize scattering from an adiabatic taper defining the confinement of the acoustic mode. Acoustic metamaterials have also been used to focus acoustic waves while minimizing reflections, but also offer a complex fabrication process and increase device footprint [51].

The FIDT has been used to generate a focused acoustic mode by adding a radius of curvature to a standard IDT. The key design parameters and geometry that define the FIDT used in this work are shown in Fig. 4(a), showing that propagation will

Authorized licensed use limited to: Northeastern University. Downloaded on January 29,2025 at 17:02:16 UTC from IEEE Xplore. Restrictions apply.

(a)

occur in $\pm\hat{y}$, with the focusing occurring in $-\hat{y}$, where $\hat{y}$ is the y-directed unit vector. Gaussian beam formalism for Lamb waves in suspended piezoelectric films has been analyzed and applied to the FIDT structure [28], meaning the response is analogous to that of a Gaussian beam in the optical domain. For a collimated beam of light that diverges slowly as it propagates, its wave function that describes the beam is a solution of the paraxial wave equation [52], [53]. Its solution has the form of the following equation:

$$\vartheta(x, y,z,t) = \mathrm{E}(x, y,z,t)e^{j(\omega t+ky)}$$

$$\mathrm{E}_o(x, y,z) = \frac{A}{\sqrt{w(x2y+)^2z2)}} e^{\frac{jk(2xR2(+y)z2)}{}} e^{j\varphi(y)} \quad (2)\ w(y)$$

Here, $\mathrm{E}_o(x, y,z)$ is the zero-order solution of the paraxial wave equation and represents a wave traveling in $-\hat{y}$. The key characteristics of the beam are defined by $w(y)$, $R(y)$, and $\varphi(y)$ which describe the beam radius, radius of curvature for constant phase fronts, and the Gouy phase, respectively, with A controlling the magnitude of the spherical wavefront of the beam. There is also the Rayleigh range, y_R, which determines the range over which the beam can propagate without diverging significantly, or the distance in which the beam waist has increased by a factor of $\sqrt{2}$, causing the beam area to double. Mathematical descriptions of characteristics shown in (2) are defined in the following equation:

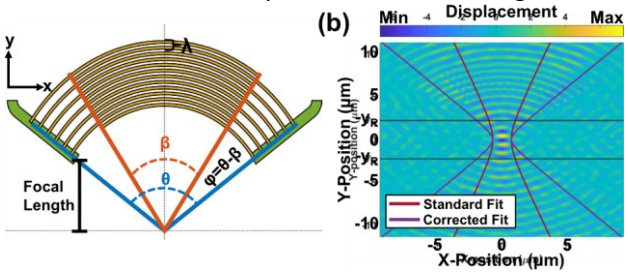

Fig. 4. (a) Geometry of and key parameters defining the focusing interdigitiated transducer. (b) Response at FIDT resonance for the Sezawa mode, shown by the out-of-plane (z-directed) displacement with the standard and corrected fitting of a beam radius for a Gaussian beam.

$$y_R = \frac{\pi w_{o2}}{\lambda}$$

$$w(y) = w_o \sqrt{1 + \left(\frac{y}{y_R}\right)^2} = w_o \sqrt{1 + y_{R2}}$$

$$R(y) = y\left(1 + \frac{y_{R2}}{y}\right)$$

$$\varphi(y) = \frac{y}{y_R}. \quad (3)$$

In (3), w_o represents the nominal beam waist. The solution described directly applies to Gaussian beams in 3-D space and is ultimately derived from Green's function solution for the 3-D Helmholtz wave equation. As SAWs are confined to the surface of the piezoelectric film, a 2-D Gaussian beam is a better approximation, and Green's function solution to the Helmholtz wave equation is defined by a Hankel function of the second kind, $H_v^{(2)}$. When applying an asymptotic expansion, the 2-D focused Gaussian beam mathematically has the same beam radius and radius of curvature, with differences coming in the amplitude and the Gouy phase shift, which gets scaled by a factor of 0.5 [28].

There also lies a difference in the nature of the beam radius between the pattern of a Gaussian optical beam and that produced by an FIDT since the transducer design itself will control the beam radius. A correction factor, α, can be introduced based on the design parameters of the FIDT to scale the beam radius based on the size of the transducer, such that

$$w(y) = w_o \sqrt{1 + \alpha\left(\frac{y}{y_R y_R F_{L2} - (y_R w_o)_2}\right)^2}$$

$$\alpha = \frac{\left(2\tan\left(\frac{\theta}{2}\right)\right)^2}{(w_o F_L)^2}. \quad (4)$$

The radius of curvature, $R(y)$, is a function of the transducer wavelength and remains unchanged. An FIDT with $\lambda = 1\ \mu$m, $\vartheta = 95^\circ$, $\varphi = 15^\circ$, and $F_L = 2\ \mu$m was simulated on the SoS material stack in an approximately semi-infinite plane. The out-of-plane (z-directed) displacement is displayed at the resonant frequency of the FIDT in Fig. 4(b), with the standard and corrected fit of the beam radius plotted over the response, with the assumption that the mode would converge to a nominal waist size of $w_o = \lambda$. The response indicates that the radius of curvature approaches infinity at the focal point of the transducer, and inside the Rayleigh range, there is a plane wave with little to no radius of curvature. Adding the correction factor allows to fully capture the physical response and propagation characteristics of the 2-D Gaussian beam produced by the FIDT.

B. Piezoelectric Etch Defined Acoustic Waveguides

An advantageous property of the FIDT is the ability to generate a wavelength-scale mode conversion with a higher intensity compared with the standard IDT. With the introduction of an acoustic waveguide, the FIDT allows for the injection of more acoustic power into the waveguide. Acoustic waveguides in slow-on-fast platforms can be defined through an etch of the piezoelectric film. A tapered etch allows for a compact means of minimizing the mode profile of the launched acoustic wave while mitigating scattering losses. By

Authorized licensed use limited to: Northeastern University. Downloaded on January 29,2025 at 17:02:16 UTC from IEEE Xplore. Restrictions apply.

(a)

placing the acoustic waveguide in the Rayleigh range of the FIDT (ideally at the focal point), a plane wave can be injected into the waveguide for PnIC applications.

COMSOL Multiphysics was utilized to calculate the amount of power injected into an acoustic waveguide for an FIDT with the same design parameters used in Fig. 4(b) and a standard IDT. The conventional IDT was designed with an electrode aperture equivalent to the projection of the FIDT aperture onto the *x*-axis at a radius equal to the focal length. The acoustic Poynting vector, $\vec{S}$, defines the mechanical energy flux, or power density and is represented by the following equation in terms of the velocity vector ($\vec{v}$) and stress tensor (T):

$$\vec{S} = \frac{-\vec{v}^{*} \cdot T}{2}. \tag{5}$$

The acoustic power injected into the waveguide, P_I, is defined by the integral of the component of the Poynting vector that is normal to input surface of the waveguide, mathematically, described in (6). The vector that describes the input surface of the waveguide with cross-sectional area *A* is $\hat{n}$

$$P_I = \int_A \vec{S} \cdot \hat{n}\, dA. \tag{6}$$

For a designated propagation in the $-\hat{y}$-direction, the *xz* plane contains the input surface of the acoustic waveguide. The piezoelectric etch defined waveguide is implemented in COMSOL Multiphysics with the out-of-plane displacement for $-\hat{y}$ directed propagation shown for the FIDT and standard IDT in Fig. 5(a) and (b), respectively. In addition, the Poynting vector is shown at the input of the waveguide, giving a visual representation of how much acoustic energy is flowing in the direction of propagation. This indicates that there is more scattering occurring for standard IDT compared with the FIDT, and confirmed through a plot of the injected power over the resonant frequency band of the transducer shown in Fig. 5(c). Injected power is normalized against the capacitance of the respective transducer to directly compare the two designs. Over this resonant frequency band, P_I is, on average,

Authorized licensed use limited to: Northeastern University. Downloaded on January 29,2025 at 17:02:16 UTC from IEEE Xplore. Restrictions apply.

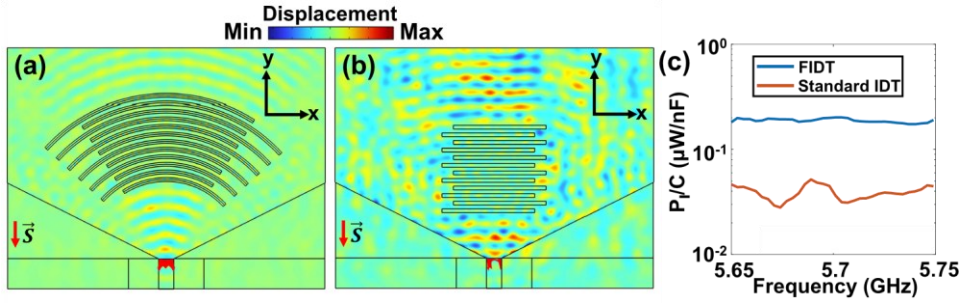

Fig. 5. Out-of-plane (z-directed) displacement in (a) FIDT structure and (b) IDT structure, with $\vec{S}$ being the acoustic Poynting vector at the input cross section of the piezoelectric defined waveguide. (c) Acoustic power injected (P_I) into the acoustic waveguide over the resonant frequency band of the FIDT and standard IDT configurations, normalized against the capacitance of each respective transducer.

a full order of magnitude higher for the FIDT compared to the standard IDT. For PnIC applications that require the wavelength-scale conversion and minimization of acoustic mode profiles, FIDTs serve as a great candidate toward the realization for phononic devices, thanks to their ability to inject larger amounts of power into acoustic waveguides.

C. Identity Mapping for DoFs Reduction

Numerical modeling of full 3-D IDT structures often desires a large amount of computational resources and time. In order to capture the appropriate behavior of the transducer, the largest mesh element size must be set to be much smaller than one wavelength ($\lambda/12$ being ideal). For the modeling of the transducers alone, these models will begin to posses several hundreds of thousands of degrees of freedom (DoFs). The response of the FIDT is a necessity for launching a focused mode into an acoustic waveguide, but as these models are developed toward larger scale PnIC devices, the resources needed to computationally solve the multiphysics problem will become unattainable.

Identity mapping using COMSOL is an effective way of retaining the response of the FIDT while simultaneously reducing the number of DoF. This mapping allows for the implementation and simulation of phononic devices and components without the repeated simulation of the transducer response. First, the response of the transducer is simulated (with all of the necessary boundary conditions). A second component is defined such that the geometries would overlap if observed in the same coordinate axes, allowing the output response of the transducer to be used as input prescribed displacement boundary conditions for the excitation of an acoustic waveguide. It is imperative to have the meshing at this boundary of components be equal to each other. After the response of the transducer is simulated one single time, the response of more intricate phononic devices can be analyzed in a more time- and computational-effective manner. For example, the response of the Sezawa mode launched from the same transducer design seen in Fig. 5(a) is mapped to observe the mode propagation across the waveguide, and is seen in Fig. 6(a). In this case, a ratio ζ is defined to capture the ratio of the out-flowing power to the in-flowing power of the acoustic waveguide, which is visualized in Fig. 6(b). It should be noted that the Poynting vector is heavily dependent on gradients, and

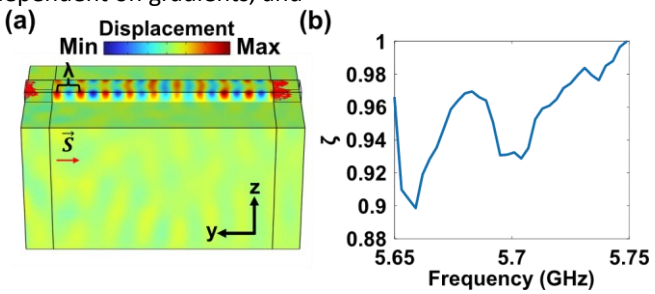

Fig. 6. (a) Excitation of Sezawa mode in an acoustic waveguide from identity matching in COMSOL, demonstrating propagation and confinement within the waveguide. (b) Ratio showcasing the amount of acoustic power flowing out of the waveguide relative to the input power, demonstrating minimal power loss and high confinement.

therefore for mesh sizes too coarse, a value of the out-flowing power can be computed to be larger than that of the in-flowing power. The use of identity mapping reduces the number of DoFs by roughly 1.5 million, retaining the same response as the full simulation.

V. Experimental Results

To validate the results observed in FEM simulations, ADLs using standard and focusing IDTs were fabricated and directly compared against each other. A relatively simple two-mask fabrication process is completed for the analysis of FIDTs for the use of PnICs in the 30% SoS platform. Devices were fabricated with wavelengths corresponding to t/λ of 0.10, 0.15, and 0.20 to evaluate the effects of mode dispersion across the ADLs.

A. Fabrication Process

The fabricated material stack employed consists of 500 nm of 30% ScAlN deposited using RF-magnetron sputtering from a casted target demonstrated in Fig. 7(a-i). X-ray diffraction (XRD) scans were used to generate a rocking curve that showcased a full-width at half-maximum (FWHM) of 2.40°. Top LFE electrodes and probing pads were patterned using the Heidelberg DWL 66+ followed by the lift-off of 10-nm Ti and 150-nm Au, as shown in Fig. 7(a-ii). The acoustic waveguides

Authorized licensed use limited to: Northeastern University. Downloaded on January 29,2025 at 17:02:16 UTC from IEEE Xplore. Restrictions apply.

were subsequently formed through an Ar-based ion mill etch of the ScAlN film, as shown in Fig. 7(a-iii), for the completion of the two-mask fabrication process. A standard ADL with

Fig. 7. (a) Fabrication of ADLs demonstrating: (i) RF magnetron sputtering of 500 nm of 30% SoS, (ii) electron-beam evaporation of 150-nm gold LFE electrodes, and (iii) Ar-based ion mill etch through the ScAlN film. Optical image showing a sample (b) standard and (c) FIDT ADL.

$\lambda = 5\ \mu$m, an electrode aperture of 10λ, 32 electrode pairs, and a delay line length (defined as center-to-center of input-tooutput transducer) of 300 μm is shown in Fig. 7(b). Similarly, the design of an FIDT ADL with a $\lambda = 5\ \mu$m, focal length of 20 μm, 20 electrode pairs, waveguide length of 200 μm, and a waveguide width of 4λ is shown in Fig. 7(c), demonstrating the devices to be compared.

B. Acoustic Delay Lines

The dominating performance parameters of ADLs in RF characterization are demonstrated in the device insertion loss and propagation loss (PL). For the application of PnICs, the overall size and complexity of these devices and systems will be limited by the inherent attenuation of acoustic signals as governed by the material properties, indicating the importance of PL. Impedance matching devices to 50-Ω eliminates electrical losses and facilitates direct comparison between devices. The raw response of an ADL with $\lambda = 2.5\ \mu$m, 16 electrode pairs, aperture of 25λ, and delay line distance of 750 μm is shown in Fig. 8(a). The initial consideration is that the insertion loss is very high and the excursion of the forward transmission is poor. As acoustic waves propagate, the launched beam will experience diffraction or spatial spreading [54]. Specifically, beam spreading that is due in part to aperture diffraction occurs when the propagation distance is comparable to $(w^2/2\lambda)$, where w represents the transducer aperture or active length [55]. The standard delay lines (SDLs) in this work have a maximum aperture of 25λ, indicating that there should be significant diffraction due to transducer design. Conjugate matching of the transducer can be performed from the analysis of the impedance and admittance of the transducer response through Z_{11} and Y_{11} [56], with these

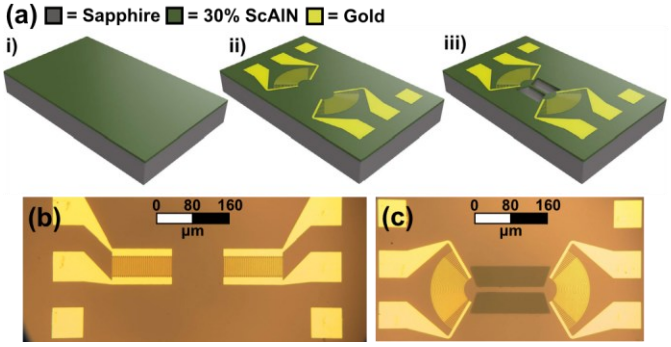

responses shown in Fig. 8(b). The constant offset on the real component of the transducer impedance indicates the resistance. Subsequently, the slope of the dashed black line, a result of fitting the admittance linearly to regions outside of the resonant band, represents the transducer capacitance. To conjugate match to 50-Ω termination, a simple resistor–inductor network can be artificially inserted into the device under test (DUT), as indicated in Fig. 8(c). Since these acoustic modes have known phase and group velocities, the S-parameters can be windowed in time to mitigate any reflections for a definite

Fig. 8. (a) Raw S_{11} and S_{21} for selected ADL. (b) Real and imaginary components of transducer impedance and admittance for the extraction of resistance and capacitance to implement conjugately matched network. (c) Schematic demonstrating formulation of simulated conjugate matched network. (d) 50-Ω matched response of sample ADL.

response through the use of an inverse Fourier transform. Finally, the matched and time-gated ADL response can be seen through S_{11} and S_{21} for the extraction of insertion loss over delay line length, as demonstrated in Fig. 8(d).

Fabricated delay lines in this work were designed to operate at multiple t/λ values, with wavelengths corresponding to 5.00, 3.33, and 2.50 μm. To demonstrate the performance over operating wavelength (and frequency), the reflection (S_{11}) and transmission (S_{21}) are plotted for varying t/λ for both SDLs and FIDT delay lines (FDLs) for the fundamental Rayleigh mode, as demonstrated in Fig. 9(a) and (b), respectively. Similarly, the responses for the Sezawa mode are shown in Fig. 9(c) and (d). Fractional bandwidth (FBW) is critical in filter performance and suitability for specific applications.

A 10-dB FBW is computed through FBW = $(f_2 - f_1/f_c)$. The center frequency of the passband f_c represents the frequency of maximum transmission and f_1(f_2) the frequency 10-dB lower than the minimum insertion loss at a frequency lower (higher) than f_c. PL extraction is performed through a linear fit of the minimum insertion loss over delay line length. The SDLs were fabricated to have delay line lengths from 50 to 750 μm with the length defined as the distance between the center of the two transducers. Similarly, the FIDT delay lines were fabricated to have the same delay line lengths, with the distance being defined as the length of the acoustic waveguide. The FIDTs were fabricated with a focal length of 20 μm and ϑ (φ) of 120° (15°).

A summary of both sets of devices can be found for the SDLs

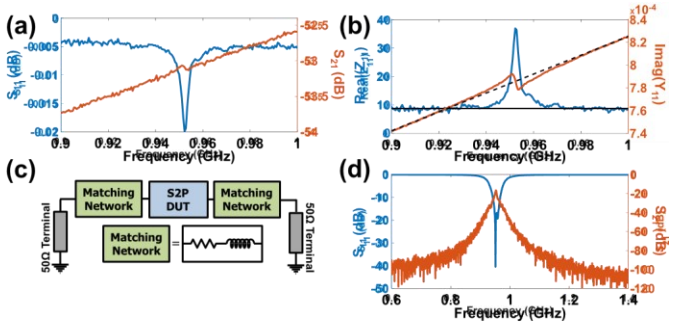

and FDLs in Tables II and III, respectively, showing the key performance metrics (PL and average FBW across delay line length variations) for PnICs. Table II shows the fabricated variations of uniform aperture transducers and the delay line

Authorized licensed use limited to: Northeastern University. Downloaded on January 29,2025 at 17:02:16 UTC from IEEE Xplore. Restrictions apply.

TABLE II

RESULTS SUMMARY FOR FABRICATED SDLS

Standard Delay Lines												
NP	**16**				**32**				**64**			
Aperture	**10λ**		**25λ**		**10λ**		**25λ**		**10λ**		**25λ**	
λ (μm)	**PL (dB/mm)**	**FBW (%)**	**PL (dB/mm)**	**FBW (%)**	**PL (dB/mm)**	**FBW (%)**	**PL (dB/mm)**	**FBW (%)**	**PL (dB/mm)**	**FBW (%)**	**PL (dB/mm)**	**FBW (%)**
5.00	36.00	2.39	34.73	1.34	37.66	1.04	32.81	0.89	32.91	1.15	28.13	0.61
3.33	29.58	4.46	28.52	3.86	29.37	4.06	25.93	2.50	18.16	5.06	27.11	6.64
2.5 (Rayleigh)	29.94	5.06	33.60	6.49	33.70	7.17	33.13	5.54	33.02	6.17	32.23	5.31
2.5 (Sezawa)	24.04	5.71	12.77	6.68	12.09	3.55	9.88	3.54	8.88	2.57	4.44	2.59

TABLE III

RESULTS SUMMARY FOR FABRICATED FOCUSING DELAY LINES

Focusing Delay Lines								
WG$_w$	**λ/2**		**λ**		**2λ**		**4λ**	
NP	**20**		**20**		**20**		**20**	
λ (μm)	**PL (dB/mm)**	**FBW (%)**	**PL (dB/mm)**	**FBW (%)**	**PL (dB/mm)**	**FBW (%)**	**PL (dB/mm)**	**FBW (%)**
5.00	32.21	2.47	27.77	1.53	25.66	1.91	31.38	2.35
3.33	32.58	1.52	26.48	1.47	18.32	2.00	21.4	1.74
2.5 (Rayleigh)	30.04	4.18	33.81	4.21	18.27	3.58	27.70	7.64
2.5 (Sezawa)	5.65	10.84	10.44	10.44	10.08	12.21	6.92	6.06

performance highlighted by the PL and FBW. Immediately, it is clear that the PL is improved across a singular wavelength with the increasing electrode aperture, indicating a higher amount of acoustic energy transduced from improved impedance matching. These delay lines also suffer from a significantly higher PL compared with the previous work [33], likely due to diffraction at the transducer from the small aperture size. From the dispersion relation in Fig. 2, the coupling will increase for both the fundamental Rayleigh and Sezawa modes with the increasing t/λ. As the wavelength decreases, there is an increase in the average FBW, coupled with a lower PL, following the trend that FBW will improve with higher coupling [57].

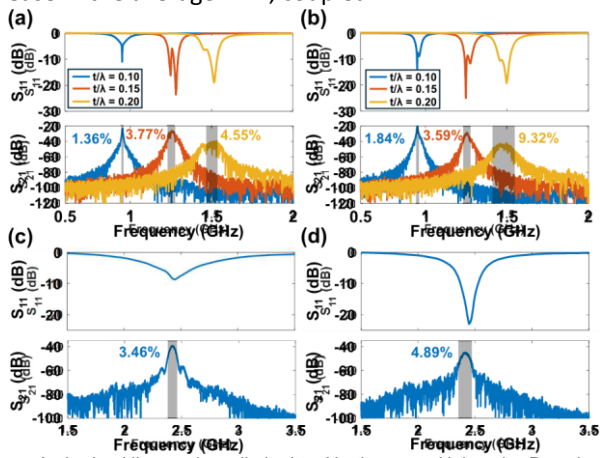

Fig. 9. Time-gated and impedance matched reflection (S_{11}) and transmission (S_{21}) sweeping t/λ for (a) standard and (b) FDLs highlighting the FBW at each operating frequency. Similarly, the Sezawa mode transmission and reflection at a t/λ of 0.2 is shown for (c) standard and (d) FDLs, highlighting the FBW of each.

A summary of the FDLs is shown in Table III with variations in the acoustic waveguide width. The PL and average FBW are again summarized over transducer variation. PL does not follow a constant trend, indicating the potential presence of a waveguide width that corresponds to a single-mode acoustic waveguide and other higher order SAW modes [58]. The summaries in Tables II and III show that the FIDTs for an ADL application are able to maintain their performance compared with the standard tranducers, while simultaneously converging the SAWs to a wavelength scale for the mode injection to an acoustic waveguide, a necessity for compact phononic circuits.

The presence of the Sezawa mode with the inherently higher phase velocity compared with the fundamental Rayleigh allows for the ease of frequency scaling given the same lithographic constraints. The Sezawa mode is also cutoff for t/λ

Authorized licensed use limited to: Northeastern University. Downloaded on January 29,2025 at 17:02:16 UTC from IEEE Xplore. Restrictions apply.

less than 0.2, and the results for both are reflected in the tables. The results can easily be improved by fabricating devices with optimal coupling, electrode configuration, and transducer design for impedance matching for the implementation of phononic devices and PnICs, including bends [30], ring resonators [19], and other acoustic devices meant to emulate what is seen in the photonic domain for signal processing systems. Enabled by the use of FIDTs and etchdefined waveguides, guided SAWs prove to have potential for compact RF applications.

VI. Conclusion

In summary, the dispersion relation was investigated for guided SAWs in 30% SoS in terms of the coupling (as a function of electrode configuration), phase velocity, and mode confinement for a swept t/λ. Numerically and analytically modeling FIDTs and their responses yielded the realization of wavelength-scale conversion of these SAWs for the injection of energy into etch-defined acoustic waveguides. Offering the advantage of naturally focusing the mode with superior energy injection yields promising applications for communication and computing systems. Both standard and focusing transducers were used in the application of ADLs for the summary of PL and FBW.

The use of FIDTs and wavelength-scale conversion allows for compact and interconnected large-scale systems that cannot be achieved using standard transducers. Moreover, the utilization of acoustic waveguides for the spatial manipulation of SAWs opens avenues for the creation of a device library that is analogous to the photonic domain, as well as applications for topological waveguides [59]. Alternative platforms can also be employed that use faster piezoelectrics on slower substrates for increased coupling, and therefore device performance [60]. Overall, the analysis of both the fundamental Rayleigh and Sezawa guided modes in 30% SoS proves to be a robust platform for the development of large scale PnICs for the development of compact and on-chip signal processing systems.

References

[1] H. Bhugra and G. Piazza, Eds., *Piezoelectric MEMS Resonators* (Microsystems and Nanosystems). Cham, Switzerland: Springer, 2017.

[2] G. Giribaldi, L. Colombo, P. Simeoni, and M. Rinaldi, "Compact and wideband nanoacoustic pass-band filters for future 5G and 6G cellular radios," *Nature Commun.*, vol. 15, no. 1, p. 304, Jan. 2024.

[3] R. Ruby, "A snapshot in time: The future in filters for cell phones," *IEEE Microw. Mag.*, vol. 16, no. 7, pp. 46–59, Aug. 2015.

[4] T. Murata, M. Kadota, T. Nakao, and K. Matsuda, "Surface acoustic wave filter in high frequency with narrow bandwidth and excellent temperature characteristic," in *IEEE MTT-S Int. Microw. Symp. Dig.*, Atlanta, GA, USA, Jun. 2008, pp. 1255–1258.

[5] W. Soluch, "Design of SAW delay lines for sensors," *Sens. Actuators A, Phys.*, vol. 67, nos. 1–3, pp. 60–64, May 1998.

[6] S. Tanaka, K. Park, and M. Esashi, "Lithium-niobate-based surface acoustic wave oscillator directly integrated with CMOS sustaining amplifier," *IEEE Trans. Ultrason., Ferroelectr., Freq. Control*, vol. 59, no. 8, pp. 1800–1805, Aug. 2012.

[7] T. Manzaneque, R. Lu, Y. Yang, and S. Gong, "An SH0 lithium niobate correlator for orthogonal frequency coded spread spectrum communications," in *Proc. Joint Conf. Eur. Freq. Time Forum IEEE Int. Freq. Control Symp. (EFTF/IFCS)*, Besancon, France, Jul. 2017, pp. 143–147.

[8] S. Ghosh and J. Cafarella, "SAW correlators in $LiNbO_3$ and GaN on sapphire," in *Proc. IEEE Int. Freq. Control Symp. (IFCS)*, May 2018, pp. 1–4.

[9] S. Ghosh and M. Ricci, "A 3-port circulator based on non-reciprocal acoustoelectric delay lines," in *Proc. Joint Conf. IEEE Int. Freq. Control Symp. Int. Symp. Appl. Ferroelectr. (IFCS-ISAF)*, Keystone, CO, USA, Jul. 2020, pp. 1–3.

[10] M. Kadota et al., "SAW substrate for duplexer with excellent temperature characteristics and large reflection coefficient realized by using flattened SiO_2 film and thick heavy metal film," in *IEEE MTTS Int. Microw. Symp. Dig.*, San Francisco, CA, USA, Jun. 2006, pp. 382–385.

[11] R. Lu, J. Krol, L. Gao, and S. Gong, "A frequency independent framework for synthesis of programmable non-reciprocal networks," *Sci. Rep.*, vol. 8, no. 1, p. 14655, Oct. 2018.

[12] S. Ghosh, M. A. Hollis, and R. J. Molnar, "Acoustoelectric amplification of Rayleigh waves in low sheet density AlGaN/GaN heterostructures on sapphire," *Appl. Phys. Lett.*, vol. 114, no. 6, Feb. 2019, Art. no. 063502.

[13] S. Ghosh, "Acoustic wave amplification with thin film silicon bonded on lithium niobate," *J. Micromech. Microeng.*, vol. 32, no. 11, Nov. 2022, Art. no. 114001.

[14] L. Shao et al., "Phononic band structure engineering for high-Q gigahertz surface acoustic wave resonators on lithium niobate," *Phys. Rev. Appl.*, vol. 12, Jul. 2019, Art. no. 014022.

[15] S. Zhang et al., "Surface acoustic wave devices using lithium niobate on silicon carbide," *IEEE Trans. Microw. Theory Techn.*, vol. 68, no. 9, pp. 3653–3666, Sep. 2020.

[16] M. Kadota and S. Tanaka, "Wideband acoustic wave resonators composed of hetero acoustic layer structure," *Jpn. J. Appl. Phys.*, vol. 57, no. 7S1, Jul. 2018, Art. no. 07LD12.

[17] B. A. Auld, *Acoustic Fields and Waves in Solids. 1*. 2nd ed. Melbourne, FL, USA: Krieger, 1990.

[18] T. Aubert et al., "Non-leaky longitudinal acoustic modes in $Sc_xAl_{1-x}N$/sapphire structure for high-temperature sensor applications," *Appl. Phys. Lett.*, vol. 115, Aug. 2019, Art. no. 083502.

[19] M. Bicer, S. Valle, J. Brown, M. Kuball, and K. C. Balram, "Gallium nitride phononic integrated circuits platform for GHz frequency acoustic wave devices," *Appl. Phys. Lett.*, vol. 120, no. 24, Jun. 2022, Art. no. 243502.

[20] I. Ahmed, U. Rawat, J.-T. Chen, and D. Weinstein, "Super-highfrequency low-loss sezawa mode SAW devices in a GaN/SiC platform," 2022, *arXiv:2204.12113*.

[21] M. A. Caro et al., "Piezoelectric coefficients and spontaneous polarization of ScAlN," *J. Phys., Condens. Matter*, vol. 27, Jun. 2015, Art. no. 245901.

[22] X. Zhao and C. Cassella, "On the coupling coefficient of $Sc_yAl_{1-y}N$based piezoelectric acoustic resonators," in *Proc. Joint Conf. IEEE Int. Freq. Control Symp. Eur. Freq. Time Forum (EFTF/IFC)*, Orlando, FL, USA, Apr. 2019, pp. 1–4.

[23] F. Kanouni, F. Laidoudi, S. Amara, and K. Bouamama, "Improvement of surface acoustic wave delay lines using C-Axis tilted AlScN thin film," *Acoust. Phys.*, vol. 68, no. 5, pp. 447–458, Oct. 2022.

[24] A. H. Safavi-Naeini, D. Van Thourhout, R. Baets, and R. Van Laer, "Controlling phonons and photons at the wavelength scale: Integrated photonics meets integrated phononics," *Optica*, vol. 6, no. 2, p. 213, 2019.

[25] W. Wang, M. Shen, C.-L. Zou, W. Fu, Z. Shen, and H. X. Tang, "Highacoustic-index-contrast phononic circuits: Numerical modeling," *J. Appl. Phys.*, vol. 128, no. 18, Nov. 2020, Art. no. 184503.

[26] Q. Liu, H. Li, and M. Li, "Electromechanical Brillouin scattering in integrated optomechanical waveguides," *Optica*, vol. 6, no. 6, p. 778, Jun. 2019.

[27] W. Fu et al., "Phononic integrated circuitry and spin–orbit interaction of phonons," *Nature Commun.*, vol. 10, p. 2743, Jun. 2019.

Authorized licensed use limited to: Northeastern University. Downloaded on January 29,2025 at 17:02:16 UTC from IEEE Xplore. Restrictions apply.

[28] A. Siddiqui, R. H. Olsson, and M. Eichenfield, "Lamb wave focusing transducer for efficient coupling to wavelength-scale structures in thin piezoelectric films," *J. Microelectromech. Syst.*, vol. 27, no. 6, pp. 1054–1070, Dec. 2018.

[29] J. Guida, R. Tetro, M. Rinaldi, and S. Ghosh, "Focused S0 Lamb modes for gigahertz delay lines in 30% scandium aluminum nitride," in *Proc. IEEE Int. Ultrason. Symp. (IUS)*, Montreal, QC, Canada, Sep. 2023, pp. 1–4.

[30] J. Guida, R. Tetro, M. Rinaldi, and S. Ghosh, "Compact bends and lowloss junctions for S0 Lamb modes in fully etched scandium aluminum nitride acoustic waveguides," in *Proc. IEEE 37th Int. Conf. Micro Electro Mech. Syst. (MEMS)*, Austin, TX, USA, Jan. 2024, pp. 1091–1094.

[31] F. Hadj-Larbi and R. Serhane, "Sezawa SAW devices: Review of numerical-experimental studies and recent applications," *Sens. Actuators A, Phys.*, vol. 292, pp. 169–197, Jun. 2019.

[32] J. B. Wachtman, W. E. Tefft, D. G. Lam, and R. P. Stinchfield, "Elastic constants of synthetic single crystal corundum at room temperature," *J. Res. Nat. Bureau Standards A, Phys. Chem.*, vol. 64, no. 3, p. 213, May 1960.

[33] J. Guida, G. Giribaldi, L. Colombo, M. Rinaldi, and S. Ghosh, "Solidly mounted two-dimensional guided modes in 30% scandium aluminum nitride on sapphire," in *Proc. 22nd Int. Conf. Solid-State Sens., Actuators Microsyst. (Transducers)*, Jun. 2023, pp. 2094–2097.

[34] K.-Y. Hashimoto, *Surface Acoustic Wave Devices in Telecommunications: Modelling and Simulation*. Berlin, Germany: Springer, 2000.

[35] R. Lu, M.-H. Li, Y. Yang, T. Manzaneque, and S. Gong, "Accurate extraction of large electromechanical coupling in piezoelectric MEMS resonators," *J. Microelectromech. Syst.*, vol. 28, no. 2, pp. 209–218, Apr. 2019.

[36] W. Wang and D. Weinstein, "Acoustic Bragg reflectors for Qenhancement of unreleased MEMS resonators," in *Proc. Joint Conf. IEEE Int. Freq. Control Eur. Freq. Time Forum (FCS)*, San Francisco, CA, USA, May 2011, pp. 1–6.

[37] L. Colombo et al., "Monolithic integration of X-cut leaky SAWs and electrically small antennas for RF passive wireless sensors," in *Proc. IEEE Int. Ultrason. Symp. (IUS)*, Montreal, QC, Canada, Sep. 2023, pp. 1–4.

[38] V. Pishchik, L. A. Lytvynov, and E. R. Dobrovinskaya, *Sapphire: Material, Manufacturing, Applications*. Boston, MA, USA: Springer, 2009.

[39] G. Giribaldi, L. Colombo, F. Bersano, C. Cassella, and M. Rinaldi, "Investigation on the impact of scandium-doping on the kt2 of ScxAl1xN cross-sectional Lamé mode resonators," in *Proc. IEEE Int. Ultrason. Symp. (IUS)*, Las Vegas, NV, USA, Sep. 2020, pp. 1–4.

[40] J. Zou, C.-M. Lin, C. S. Lam, and A. P. Pisano, "Transducer design for AlN Lamb wave resonators," *J. Appl. Phys.*, vol. 121, no. 15, Apr. 2017, Art. no. 154502.

[41] J. Zou and C. S. Lam, "Electrode design of AlN Lamb wave resonators," in *Proc. IEEE Int. Freq. Control Symp. (IFCS)*, New Orleans, LA, USA, May 2016, pp. 1–5.

[42] C. Cassella and M. Rinaldi, "On the origin of high couplings twodimensional modes of vibration in aluminum nitride plates," in *Proc. IEEE Int. Freq. Control Symp. (IFCS)*, Olympic Valley, CA, USA, May 2018, pp. 1–3.

[43] H. Ieki and M. Kadota, "ZnO thin films for high frequency SAW devices," in *Proc. IEEE Ultrason. Symp. Int. Symp.*, Caesars Tahoe, NV, USA, vol. 1, Oct. 1999, pp. 281–289.

[44] H. F. Tiersten, "Elastic surface waves guided by thin films," *J. Appl. Phys.*, vol. 40, no. 2, pp. 770–789, Feb. 1969.

[45] T.-H. Hsu, K.-J. Tseng, and M.-H. Li, "Thin-film lithium niobate-oninsulator (LNOI) shear horizontal surface acoustic wave resonators," *J. Micromech. Microeng.*, vol. 31, no. 5, May 2021, Art. no. 054003.

[46] Z. Feng, Y. Liu, X. Xi, L. Wang, and X. Sun, "Gigahertz phononic integrated circuits based on overlay slot waveguides," *Phys. Rev. Appl.*, vol. 19, no. 6, Jun. 2023, Art. no. 064076.

[47] T. Yamada, N. Niizeki, and H. Toyoda, "Piezoelectric and elastic properties of lithium niobate single crystals," *Jpn. J. Appl. Phys.*, vol. 6, no. 2, p. 151, Feb. 1967.

[48] C. J. Sarabalis, T. P. McKenna, R. N. Patel, R. Van Laer, and A. H. Safavi-Naeini, "Acousto-optic modulation in lithium niobate on sapphire," *APL Photon.*, vol. 5, no. 8, 2020, Art. no. 086104.

[49] M. Ishihara, T. Nakamura, F. Kokai, and Y. Koga, "Preparation of lithium niobate thin films on diamond-coated silicon substrate for surface acoustic devices," *Diamond Rel. Mater.*, vol. 12, pp. 1809–1813, Oct./Nov. 2003.

[50] F. M. Mayor, W. Jiang, C. J. Sarabalis, T. P. McKenna, J. D. Witmer, and A. H. Safavi-Naeini, "Gigahertz phononic integrated circuits on thin-film lithium niobate on sapphire," *Phys. Rev. Appl.*, vol. 15, no. 1, Jan. 2021, Art. no. 014039.

[51] M.-H. Lu, L. Feng, and Y.-F. Chen, "Phononic crystals and acoustic metamaterials," *Mater. Today*, vol. 12, pp. 34–42, Dec. 2009.

[52] G. Nienhuis, "Angular momentum and vortices in optics," in *Structured Light and Its Applications*. Amsterdam, The Netherlands: Elsevier, 2008, pp. 19–62.

[53] E. J. Galvez, "Gaussian beams in the optics course," *Amer. J. Phys.*, vol. 74, no. 4, pp. 355–361, Apr. 2006.

[54] A. J. Slobodnik, P. H. Carr, and A. J. Budreau, "Microwave frequency acoustic surface-wave loss mechanisms on $LiNbO_3$," *J. Appl. Phys.*, vol. 41, no. 11, pp. 4380–4387, Oct. 1970.

[55] T. Reeder, E. Westbrook, and D. Winslow, "Visualisation of surface acoustic waves," *Electron. Lett.*, vol. 6, no. 2, p. 30, 1970.

[56] J. Hines and D. Malocha, "A simple transducer equivalent circuit parameter extraction technique," in *Proc. IEEE Ultrason. Symp.*, Baltimore, MD, USA, vol. 1, Oct./Nov. 1993, pp. 173–177.

[57] T. Manzaneque, R. Lu, Y. Yang, and S. Gong, "Low-loss and wideband acoustic delay lines," *IEEE Trans. Microw. Theory Techn.*, vol. 67, no. 4, pp. 1379–1391, Apr. 2019.

[58] S.-J. Park, Y.-S. Joo, H.-W. Kim, and S.-K. Kim, "Selective generation of Lamb wave modes in a finite-width plate by angle-beam excitation method," *Sensors*, vol. 20, no. 14, p. 3868, Jul. 2020.

[59] X. Xu, Y. Liu, and T. Wu, "On-chip topological phononic crystal acoustic waveguide based on lithium niobate thin films," *Appl. Phys. Lett.*, vol. 124, no. 16, Apr. 2024, Art. no. 162203.

[60] X. Du, N. Sharma, Z. Tang, C. Leblanc, D. Jariwala, and R. H. Olsson, "Near 6-GHz sezawa mode surface acoustic wave resonators using AlScN on SiC," *J. Microelectromech. Syst.*, vol. 33, no. 5, pp. 577–585, Oct. 2024.

Jack Guida (Graduate Student Member, IEEE) received the B.S. degree in electrical engineering from Syracuse University, Syracuse, NY, USA, in 2021, and the M.S. degree from Northeastern University, Boston, MA, USA, in 2023, where he is currently pursuing the Ph.D. degree with the Department of Electrical and Computer Engineering.

His current research focuses on the development of phononic devices and integrated circuits in piezoelectric platforms for signal processing systems, acoustoelectric-enabled phononic circuits, and optomechanics.

Mr. Guida was a 2023 Awardee of the National Defense Science and Engineering Graduate (NDSEG) Fellowship Program.

Siddhartha Ghosh (Member, IEEE) received the B.S. degree in electrical engineering from Cornell University, Ithaca, NY, USA, in 2007, the M.S.E. degree in electrical engineering from the University of Pennsylvania, Philadelphia, PA, USA, in 2011, and the Ph.D. degree in electrical engineering from Carnegie Mellon University, Pittsburgh, PA, USA, in 2015.

From 2015 to 2020, he was a Technical Staff Member with the RF Technology Group, MIT Lincoln Laboratory, Lexington, MA, USA. Since 2021, he has been an Assistant Professor with the Department of Electrical and Computer Engineering, Northeastern University, Boston, MA, USA. His research interests include piezoelectric MEMS, optomechanical resonators, oscillator-based computing, and acoustoelectronic signal processing devices.

Authorized licensed use limited to: Northeastern University. Downloaded on January 29,2025 at 17:02:16 UTC from IEEE Xplore. Restrictions apply.

Dr. Ghosh received the DARPA Young Faculty Award in 2023 and the NSF CAREER Award in 2024.

Authorized licensed use limited to: Northeastern University. Downloaded on January 29,2025 at 17:02:16 UTC from IEEE Xplore. Restrictions apply.